THE USE OF ADJOINT METHODS FOR ADAPTIVE OBSERVATIONS

Ronald Gelaro, Rolf H. Langland, Gregory D. Rohaly
and Thomas E. Rosmond
Naval Research Laboratory
Monterey, CA USA

1. INTRODUCTION

On time scales of several days or less, numerical weather prediction can be described largely as an initial value problem. Indeed, the specification of accurate initial conditions remains one of the most important and challenging aspects of numerical weather prediction. While recent advances in atmospheric data assimilation, including the development of sophisticated variational algorithms, coupled with improvements in the quality and usage of remotely sensed data, have led to significant improvements in the overall quality of atmospheric analyses, it is generally accepted that initial condition errors remain a primary cause of major forecast failures. In data-sparse regions in particular, the rapidly growing components of analysis errors are likely to play a significant role in producing large forecast errors (Rabier et al., 1996; Gelaro et al., 1997).

Adjoint methods, developed primarily for their application to data assimilation problems in numerical weather prediction, provide an efficient means of identifying localized areas of strong initial condition sensitivity for a particular forecast situation. For example, adjoint models have been used to quantify the impact of small initial perturbations in any model variable on the development of a particular feature such as an extratropical cyclone, or to identify structures in the initial conditions that might cause large forecast errors (Rabier et al., 1996; Langland et al., 1995, Errico and Vukićević, 1992).

A recently proposed extension of the use of adjoint methods is in the development of so-called adaptive (or targeted) observing strategies, whereby it is proposed that numerical weather forecasts can be improved by incorporating additional observations in upstream data-sensitive locations. In principle, these locations can be identified in real time using singular vectors or adjoint sensitivity patterns (Langland and Rohaly, 1996; Montani et al., 1996; Palmer et al., 1997; Gelaro et al., 1997), then surveyed using a variety of relocatable (piloted or pre-programmed) observing platforms. Given the ever increasing costs of maintaining and expanding the current observational network (consider, for example, the cost of developing new remote sensing platforms), it is also appropriate to assess the value-added of various data types, especially in forecasts of weather events with significant societal

impacts. In addition, the definition of an 'optimal mix' of observing systems that provides maximum benefit to forecast skill, is also of interest when considering the design and cost of future observing networks.

Other adaptive observing strategies have been proposed based on, for example, quasi-inverse linear calculations (Pu et al., 1997), ensemble transform techniques (Bishop and Toth, 1996), and subjective identification of upper tropospheric potential vorticity (PV) maxima (Snyder, 1996). Adjoint-based strategies in particular stress the importance of sub-synoptic scale analysis errors in the middle troposphere, upscale energy cascades, and the group velocity characteristics of error propagation rather than, say, the Lagrangian advection of upper tropospheric PV maxima.

The field phase of the Fronts and Atlantic Storm Track Experiment (FASTEX), which took place during January and February 1997, provides an opportunity to assess the impact of targeted observations on the forecast skill of North Atlantic frontal cyclones in the one to three day time range. In this study, we examine the impact of adjoint-based targeted observations on cyclone forecasts during two FASTEX intensive observation periods (IOP). Targets based on singular vectors and adjoint sensitivity patterns were produced in real-time for these cases using forward and adjoint versions of the Navy Operational Global Atmospheric Prediction System (NOGAPS).

The primary platform used for adjoint-based targeted observing during FASTEX was the NOAA Gulfstream-IV (G-IV) aircraft. The G-IV provided dropsonde measurements of temperature, wind speed and direction, and relative humidity at the target locations. Unfortunately, logistical limitations which arose during field operations precluded the G-IV missions from providing adequate coverage of the upstream target areas. For this reason, we also consider GOES-8 winds and special land- and ship-based RAOBs to supplement the data coverage in the target locations, as well as to provide data in non-sensitive ("null") locations outside the target areas.

Section 2 of this paper provides a brief description of the two primary adjoint based targeting methods used during FASTEX. The important foundational principles for each method are presented and relevant practical considerations in their application are discussed. The results of assimilating targeted observations during two FASTEX IOPs are presented and analyzed in section 3. The forecast impacts of the targeted data are assessed and an interpretation of the results in terms of error projections onto the leading target structures is presented. Conclusions based on these results are presented in section 4.

2. TARGETING METHODOLOGY

The two primary adjoint-based targeted observing strategies used during FASTEX are the singular vector (SV) method (Montani et al., 1996; Palmer et al, 1997), and the gradient sensitivity (GS) method (Langland and Rohaly, 1996; Bergot et al., 1996). The two methods are similar in their basic principles and practical application; in fact, SVs and sensitivity patterns are intimately linked from a dynamical and mathematical perspective. The reader is referred to Rabier et al. (1996), Buizza et al. (1997), Palmer et al. (1997) and Gelaro et al. (1997) for detailed discussions of these topics in a more general framework. Here, we present a brief development summary which highlights the salient aspects of both targeting methods, although we focus on the SV method in presenting our case study analyses in section 3.

In the SV method, the target locations are defined by the leading (fastest growing) SVs of a linearized version of the forecast model. The SVs are solutions of the eigenvector problem

$$\mathbf{L}_\mathbf{c}^T \mathbf{P} \mathbf{L}_\mathbf{c} \, \mathbf{u}_i = \sigma_i^2 \mathbf{u}_i \,, \tag{1}$$

where $\mathbf{L}_\mathbf{c} = \mathbf{C}^{1/2} \mathbf{L} \mathbf{C}^{-1/2}$ is a transformed version of the model forward tangent propagator $\mathbf{L}$, $\mathbf{C}$ is a metric of perturbation growth, $\mathbf{L}_\mathbf{c}^T$ is the adjoint (transpose) of $\mathbf{L}_\mathbf{c}$, $\mathbf{u}_i$ are the SVs and σ_i^2 are the associated singular values (the squares of the amplification factors of the SVs).

The operator $\mathbf{P} = \mathbf{P}(s)$ in (1) is a "local projection operator" (Buizza, 1994) which confines the optimization to a pre-specified sub-volume V of the model domain such that

$$\mathbf{P}(s) = \begin{cases} 1 & \text{if } s \in V \\ 0 & \text{if } s \notin V \end{cases} \,, \tag{2}$$

where s is the location of a model grid point. We refer to V as the forecast verification area (FVA). During FASTEX, the FVA was usually defined as a localized box roughly 15°x15° centered on the forecast position of the cyclone, and extending from approximately 150 hPa to the surface. It should be noted that $\mathbf{P}$ constrains the SV calculation at the *verification time only* so as to focus the targeting impact in the FVA. There is no formal constraint on the locations of the upstream targets at the initial (analysis) time.

For the adaptive observation problem, the metric $\mathbf{C}$ should include information about the covariances of analysis errors. Since reliable estimates of these covariances are not yet readily available, a suitable alternative metric must be used. Palmer et al. (1997) have shown that a metric based on perturbation total energy is a reasonable first order approximation to the analysis error covariance metric. A total

energy metric also has appeal in that both winds and temperatures are used to validate weather forecasts, and hence measure their errors. We use this metric for the SV calculations in this study.

The resulting SVs provide an ordered set of structures which maximize the growth of perturbation energy in the FVA. The extrema of the SVs correspond to upstream locations where small changes to the initial conditions (from additional observations) can have the greatest impact on perturbation energy growth—and presumably the cyclone forecast—in the FVA.

It is worth noting some of the logistical concerns that have been raised regarding the use of SVs for adaptive observing. First, SV calculations can be computationally expensive since an iterative procedure is required to obtain the eigenvectors of the large compound operator $\mathbf{L}_\mathbf{c}^T\mathbf{P}\mathbf{L}_\mathbf{c}$. Several integrations of the forward and adjoint model are necessary to produce each eigenvector with sufficient accuracy. In addition, successive SVs may present different target areas.

In practice, these problems are ameliorated to a large extent by the fact that the targeting is done for a limited spatial domain. This greatly reduces the computational requirements since only the leading few (typically 1–3) SVs are needed to describe a significant fraction of the forecast error variance. At the same time, for a limited optimization domain, the upstream locations of these SVs are not likely to be widely separated. In the event that separate, viable targets occur, they can be prioritized based on, for example, the SV growth rates or the sparsity of conventional data.

In the GS method, the target locations are defined by the gradient of a forecast measure J with respect to the initial conditions. The gradient calculation is obtained from an adjoint model integration

$$\frac{\partial J}{\partial \mathbf{x}_0} = \mathbf{L}^T \left(\frac{\partial J}{\partial \mathbf{x}_t} \right) , \tag{3}$$

where $\partial J/\partial \mathbf{x}_t$ is the gradient of J with respect to the model state vector $\mathbf{x}_t$ at the forecast verification time, $\partial J/\partial \mathbf{x}_0$ is the gradient of J with respect to the initial conditions $\mathbf{x}_0$ (commonly referred to as the sensitivity pattern, which defines the target area), and $\mathbf{L}^T$ is the model adjoint propagator. Note that the starting condition of the adjoint integration is $\partial J/\partial \mathbf{x}_t$, rather than J itself, so that (3) relates *gradients* of J at the initial and verification times.

The utility of this calculation in general is that, given $\partial J/\partial \mathbf{x}_0$, the impact on J at the verification time due to a small change to the initial conditions $\delta \mathbf{x}_0$ *in any component of the model state vector* is given to first approximation by

$$\delta J = < \frac{\partial J}{\partial \mathbf{x}_0} ; \delta \mathbf{x}_0 > , \tag{4}$$

where $< ; >$ is the Euclidean inner-product. Thus, for example, if J were chosen based on knowledge of the forecast error, then the extrema of $\partial J/\partial \mathbf{x}_0$ show the locations where small changes to the initial conditions have the greatest impact on the forecast error.

Although in real time targeting the forecast error is of course unknown, it is instructive to consider for the moment a (diagnostic) sensitivity calculation in which J is the energy-weighted forecast error (Rabier et al., 1996)

$$J = \frac{1}{2} < \mathbf{e}_t ; \mathbf{C}\mathbf{e}_t > , \tag{5}$$

where $\mathbf{e}_t$ is the state vector forecast error at the verification time and $\mathbf{C}$ is the energy metric as in (1). With this choice of J, it is easily shown that the sensitivity can be expressed

$$\frac{\partial J}{\partial \mathbf{x}_0} = \mathbf{C}^{1/2} \sum_i \sigma_i^2 \, c_i \mathbf{u}_i \, , \tag{6}$$

where $\mathbf{u}_i$ are the total energy SVs and c_i are projection coefficients (Gelaro et al., 1997). In this case, the linkage between the SVs and the sensitivity pattern is clear; the sensitivity pattern is a linear combination of SVs weighted by the growth rates (singular vales) σ_i^2. Moreover, if the growth rate of the leading SV is dominant, then, from a targeting perspective, the SV and GS methods point to the same observing location.

In real-time adaptive observing, the aim is to define a J that represents a reasonable surrogate for the forecast error. During FASTEX, J was defined as the average vorticity in the lower-tropospheric portion (below 650 hPa) of the FVA. Analogous to the SV method, the extrema of the sensitivity pattern correspond to areas where small magnitude changes to the initial conditions have the greatest impact on the lower-tropospheric vorticity in the FVA.

Compared with the SV method, the GS method has the advantage of being computationally efficient, since it requires only a single integration of the adjoint model (which is roughly comparable in cost to a standard nonlinear forecast of the same length). In addition, for a given J, there is a unique sensitivity vector which defines the target area. However, the extent to which these targets describe the forecast error sensitivity depends on the extent to which J is correlated with the actual forecast error. In FASTEX, an appropriate choice for J was easily made since low-level vorticity is highly correlated with the cyclone forecast error. However, when targeting over larger domains, or in forecast situations that are not necessarily dominated by any one synoptic feature, then appropriate choices for J may require careful consideration.

3. TARGETING RESULTS

3.1 FASTEX IOP-18

IOP-18 is presented as a case which provides some of the most comprehensive G-IV dropsonde and GOES-8 wind data coverage of an adjoint based target during FASTEX, facilitating a proof-of-concept demonstration of key issues in adaptive observing. The early stages of the cyclone development are characterized by distinct synoptic features, including a weak to moderate low level thermal wave and associated circulation south of Greenland, and a well defined upper level jet and associated potential vorticity (PV) maximum extending northwestward toward the Labrador coast on 22 Feb 1200 UTC (not shown). The cyclone deepens from 982 hPa to 958 hPa in 24 hours, and is located south of Iceland near 20W,57N on 23 Feb 1200 UTC.

The control forecast for this case was run from initial conditions on 22 Feb 1200 UTC produced from a 6-hr (multivariate OI) data assimilation cycle containing no special FASTEX aircraft, ship or radiosonde data during the previous 24 hours. The forecast model and data assimilation scheme used are based on NOGAPS run at T79L18 resolution. The 24-hour control forecast is reasonably skillful, having the cyclone well positioned, but with a sea level pressure error of approximately 8 hPa, on 23 Feb 1200 UTC (Fig. 1). The verifying analysis at this time contains a limited number of special FASTEX observations.

We attempt to reduce the control forecast error by assimilating special FASTEX observations in regions of strong initial condition sensitivity 24 hours earlier. Fig. 2 shows the vorticity components of SV#1 at 310 and 760 hPa, and the temperature components of SV#1 and SV#3 at 760 hPa, on 22 Feb 1200 UTC. The targets shown here are based on NOGAPS SVs run at T79L18 resolution with simple physics (Rosmond, 1997). The FVA was chosen to be the volume 30W-15W, 48N-63N, 150 hPa-surface based on the forecast position of the cyclone on 23 Feb 1200 UTC. The calculation was begun from initial conditions on 21 Feb 1200 UTC, allowing a 24-hour lead time for deployment of observational resources.

The amplification rates of the three leading SVs over the 24-hour optimization interval are 5.45, 4.09 and 3.45, respectively. The primary observational target area is defined as 30W-55W, 45N-58N, which includes extrema of both temperature and vorticity for SV#1 and SV#3 on 22 Feb 1200 UTC (Figs. 2b–d). Areas of large SV amplitude over eastern Canada were considered less likely to require special observations due to the availability of conventional land based data. We note that similar target areas were identified by gradient sensitivity calculations from both NOGAPS and the French Arpege model

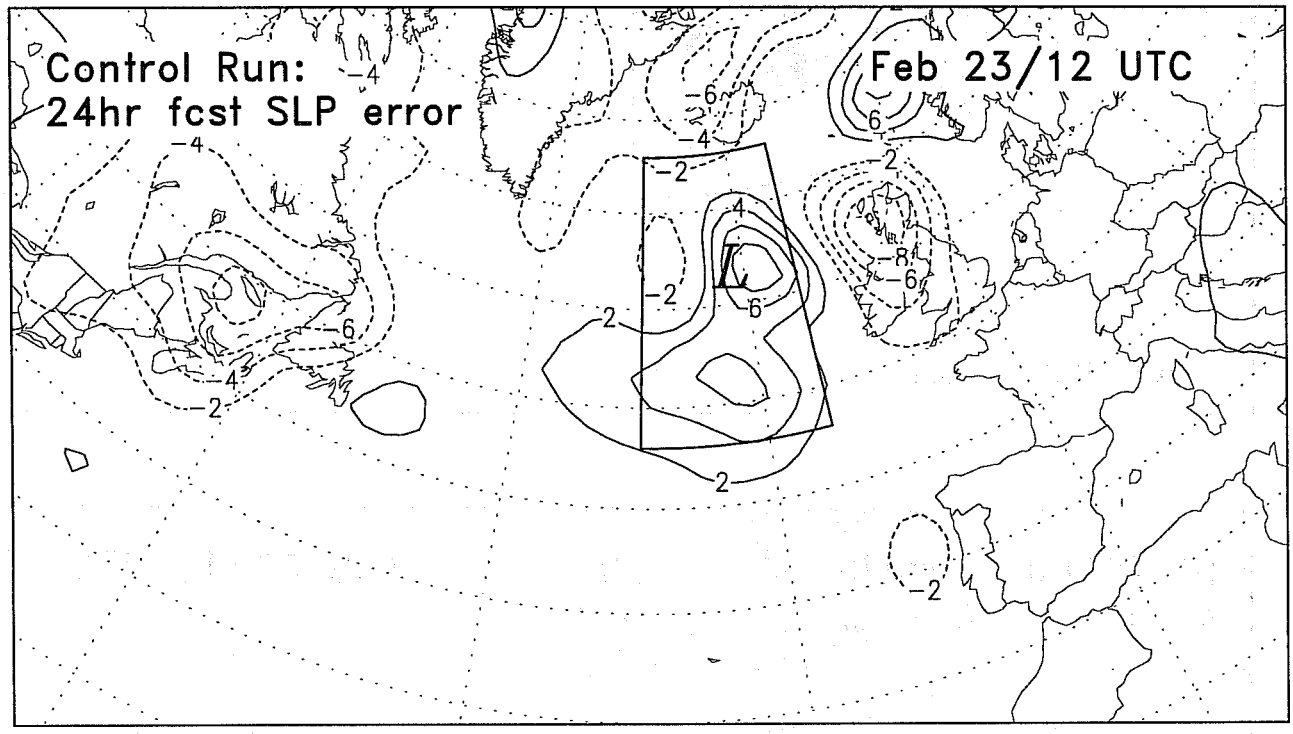

Fig.1 Sea level pressure error of the 24-hour control forecast valid 23 Feb 1200 UTC 1997 (verification time). Box outline defines the forecast verification area (FVA) used for the target calculations; L marks the control forecast position of the surface cyclone at the verification time; contour interval is 2 hPa.

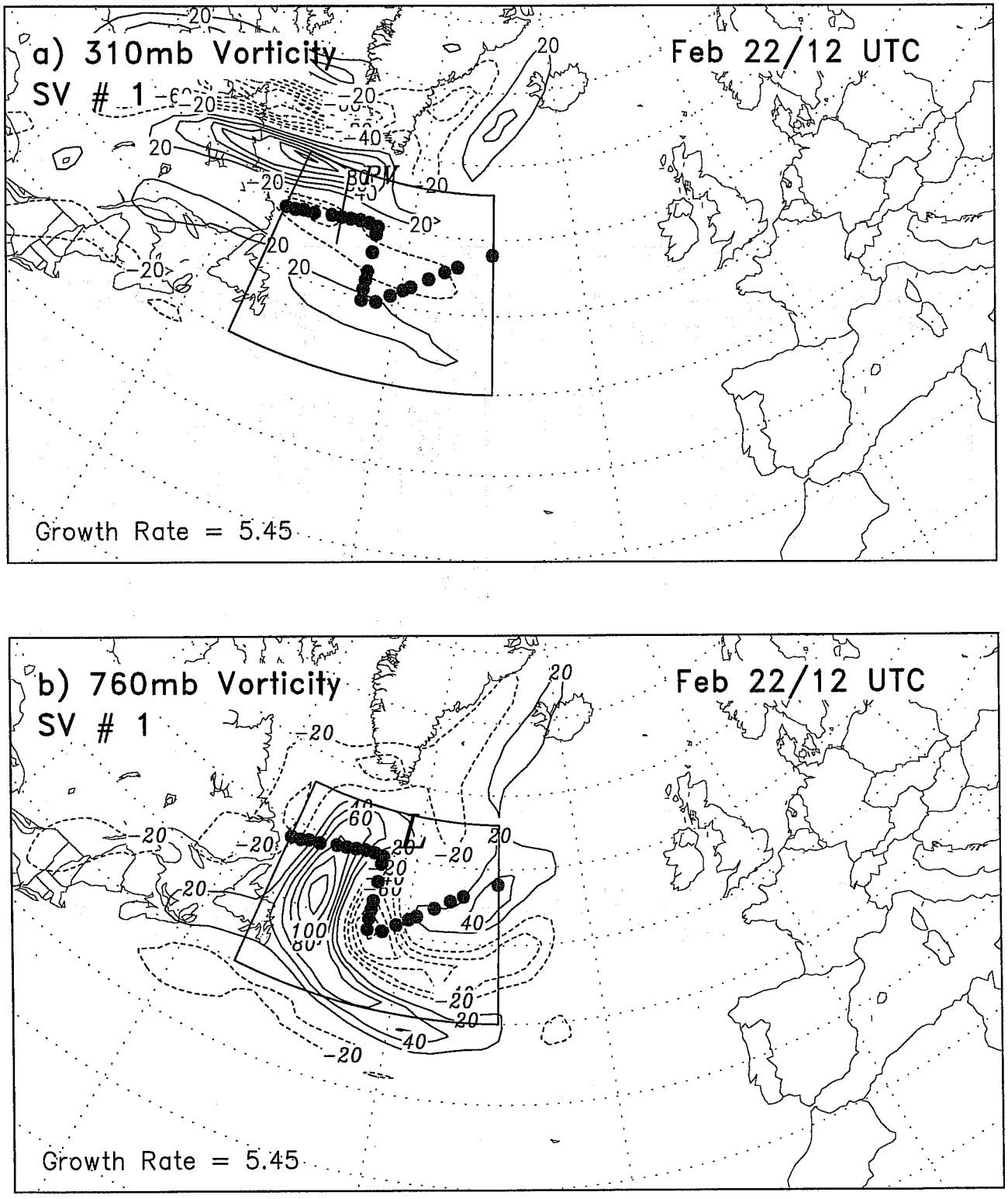

Fig. 2 Vorticity component of target SV#1 at (a) 310 hPa and (b) 760 hPa, valid 22 Feb 1200 UTC 1997 (target time); temperature component of (c) SV#1 and (d) SV#3 at 760 hPa. Box outline defines the primary observational target area for G-IV dropsondes; **L** marks the position of the surface cyclone at target time; contour interval is 20×10^{-5} s^{-1} in (a) and (b), and 3 K in (c) and (d).

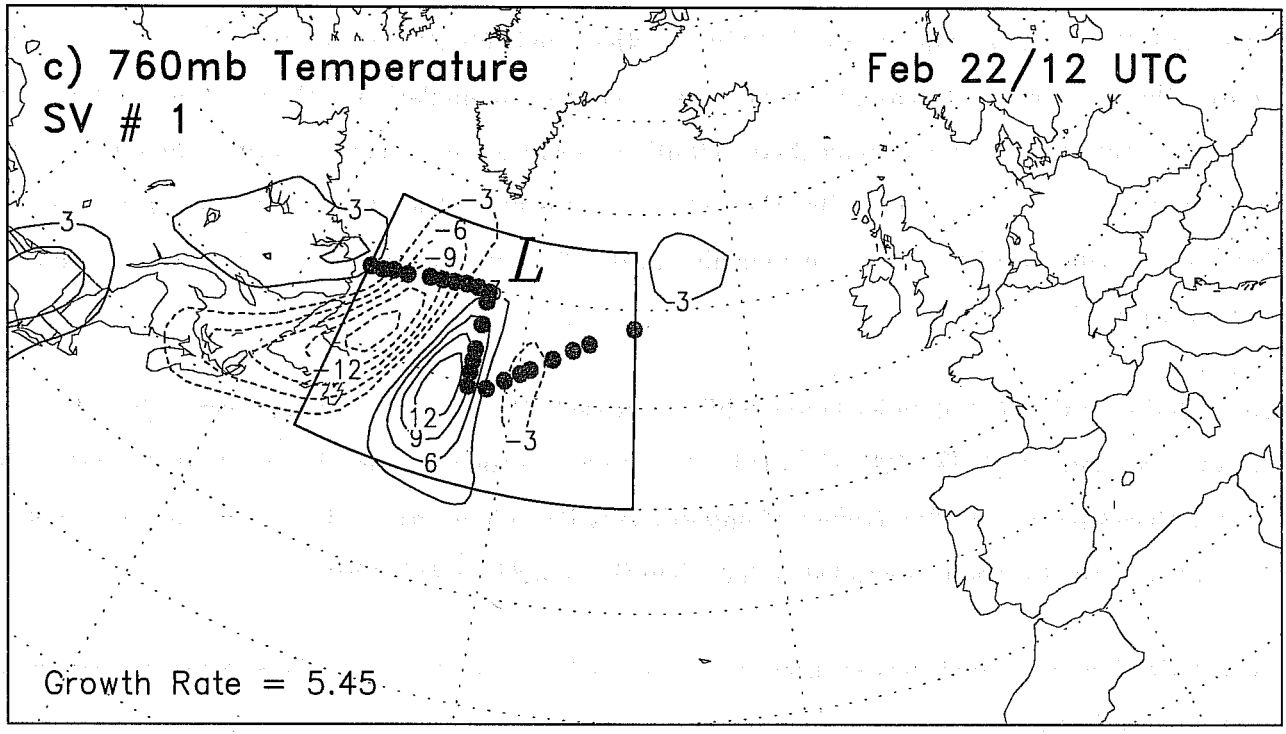

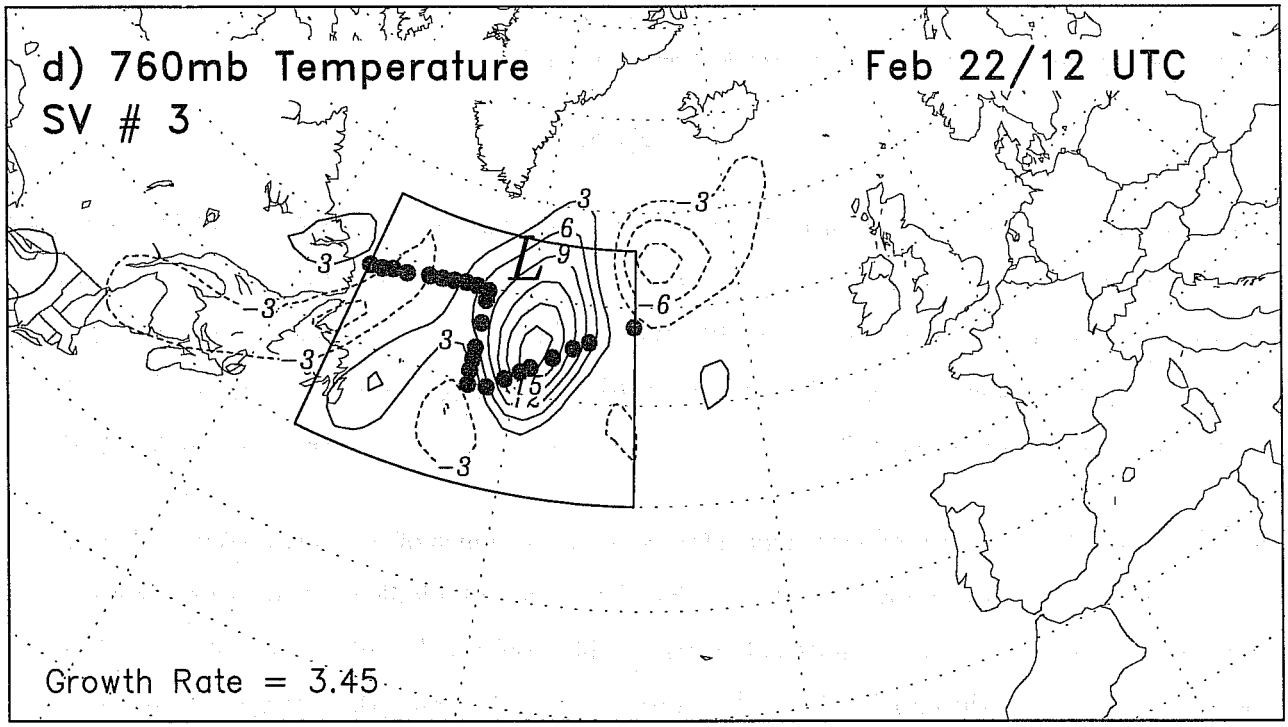

Fig. 2 (continued)

during FASTEX.

Figs. 3a,b show analysis differences of 310 hPa vorticity and 760 hPa temperature with respect to the control (hereafter referred to as increments) that result from assimilation of the G-IV dropsonde data. It appears that the analysis increments of 760 hPa temperature have a strong projection onto the SV extrema in Figs. 2c,d suggesting that the control analysis has substantial errors in the region of low level temperature sensitivity. The increments of 310 hPa vorticity appear to project onto regions of weaker sensitivity.

Assimilation of the G-IV data leads to a 6 hPa decrease in the forecast sea level pressure just south of the cyclone center on 23 Feb 1200 UTC (Fig. 3c). A comparison with Fig. 2 shows that the correction is well placed inside the FVA (values of opposite sign indicate a positive impact by the G-IV data), but has somewhat different spatial structure than the control forecast error.

A quantitative measure of forecast impact is provided by computing the change in the forecast error energy norm in the FVA, given by

$$\Delta\varepsilon_t = \frac{\varepsilon_t^{(\mathrm{exp})} - \varepsilon_t^{(\mathrm{ctl})}}{\varepsilon_t^{(\mathrm{ctl})}}, \tag{7}$$

where the superscripts denote the control and experimental (targeting) forecasts and

$$\varepsilon_t = < \mathbf{e}_t; \mathbf{C}\mathbf{e}_t > \tag{8}$$

is the forecast error norm, where $\mathbf{e}_t$ is the state vector forecast error in the FVA and $\mathbf{C}$ is defined as in (5). Note that (7) is an appropriate measure of forecast impact for these experiments because it is defined in terms of the metric used in the SV target calculation. In addition, it provides a compact measure of impact which accounts for changes in both winds and temperature in the FVA. Table 1 shows that assimilation of the G-IV dropsonde data alone reduces the forecast error norm by 25%.

The GOES-8 winds provided at least some data coverage over much of the North Atlantic during IOP-18. Although, in general, coverage can be restricted at lower and middle levels because of cloud cover, coverage at upper levels is often quite extensive. In this case, the GOES-8 coverage was sufficient to allow us to investigate the impact of additional observations in various other "target" areas. Figs. 4a,b show the increments of 310 hPa vorticity and 760 hPa temperature obtained by assimilating GOES-8 winds (only) in a much larger target area (70W-10W, 45N,60N). There are significant increments in both fields, characterized by a strengthening of the main jet and associated PV anomaly at upper levels, and strengthening of the thermal gradient in the cyclone warm sector at lower levels. These

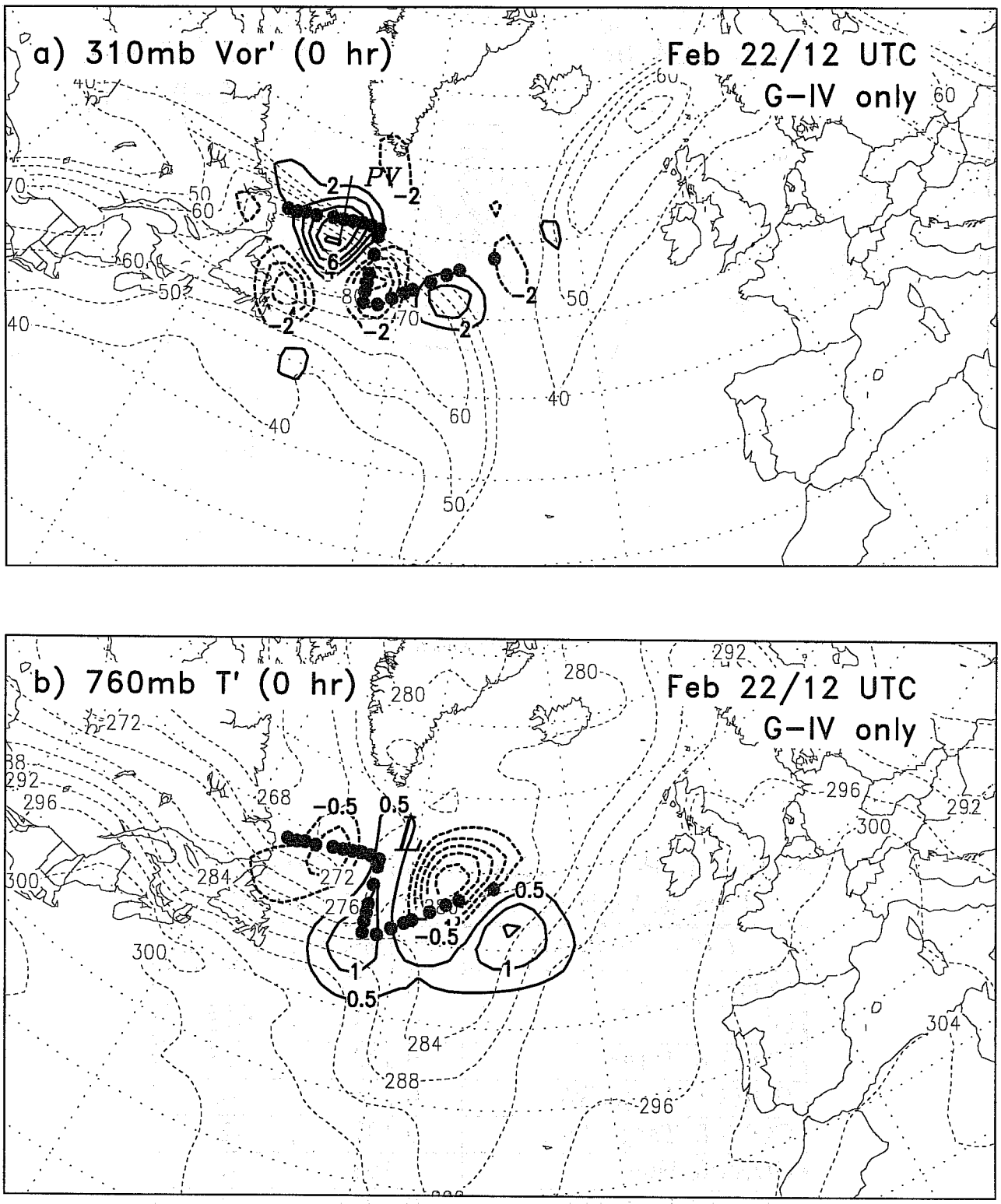

Fig. 3 Analysis increments of (a) vorticity at 310 hPa (bold contours, 2×10^{-5} s^{-1}) and (b) temperature at 760 hPa (bold contours, 0.5 K) due to assimilation of G-IV dropsonde data (solid dots) on 22 Feb 1200 UTC; (c) resulting change in 24-hour forecast sea level pressure (hPa) on 23 Feb 1200 UTC. Light dashed contours are (a) wind speed (ms^{-1}) at 310 hPa, and (b) potential temperature (K) at 760 hPa. Box outline in (c) is forecast verification area.

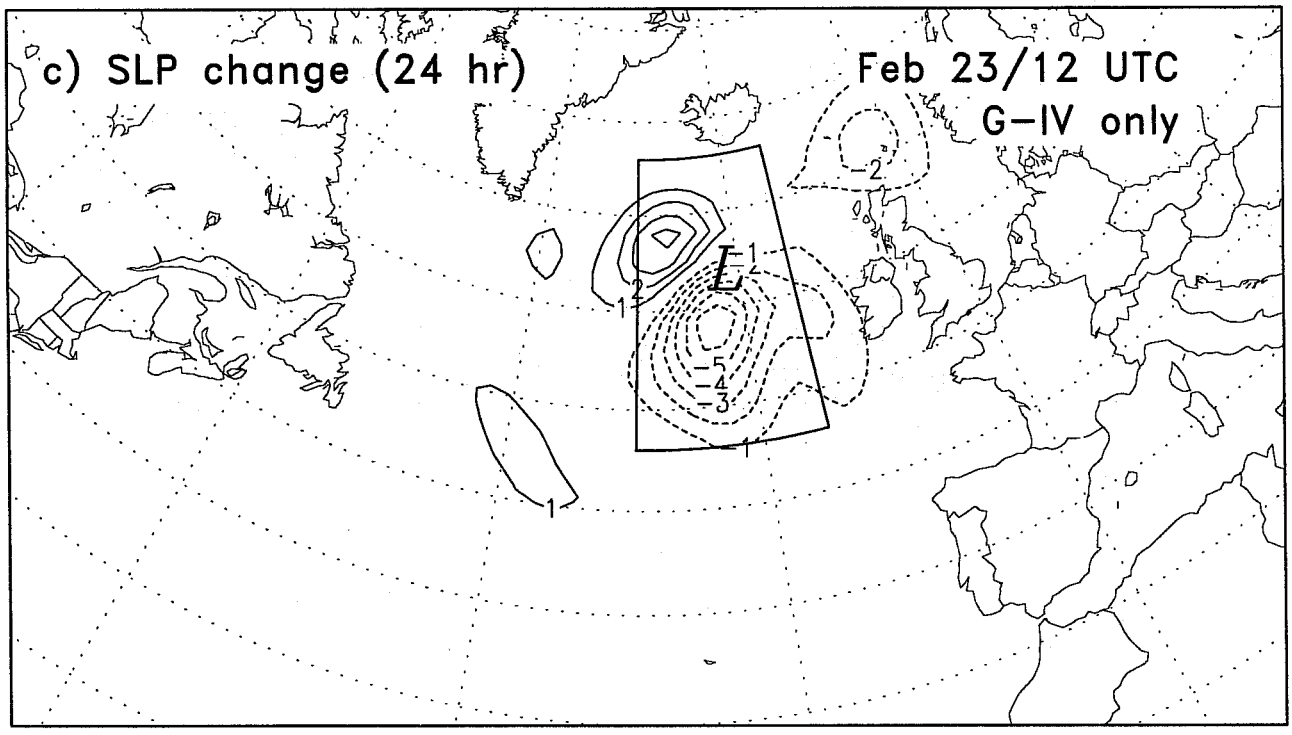

Fig. 3 (continued)

FASTEX IOP-18 22Feb 12UTC - 23Feb 12UTC

Forecast Verification Area: 30-15W, 48-63N

Initial Conditions	ε_{24} (m^2s^{-2})	$\Delta\varepsilon_{24}$ (%)
Control	0.1717	---
GIV	0.1284	-25
GOES/8 Target	0.1326	-23
GOES/8 Target/West	0.1643	-4
GOES/8 Target/East	0.1373	-20
GOES/8 Null	0.1686	-2
GIV+GOES/8 Target	0.1065	-38

Table 1: Initial condition impact on forecast error norm for data assimilation experiments in IOP-18 (see text for details).

increments are similar to those produced by assimilation of the G-IV dropsonde data. Assimilation of the GOES-8 winds in this large area reduces the forecast error norm by 23% (Table 1), roughly comparable to the reduction obtained using the G-IV dropsonde data. In contrast, when GOES-8 data are assimilated in the (null) region outside this area, the forecast error norm is reduced by only 2%.

Next, we divide the large target area into two sub-regions (indicated in Figs. 4a,b) and examine the impact of the GOES-8 winds in each of these separately. The first sub-region is defined to include the area of the main upper level jet and associated PV anomaly (*west of 40W*), while the second is defined to include the cyclone warm sector (*east of 40W*). We note that the latter includes the area where the G-IV dropsonde data made the largest changes to the low level thermal structure of the control analysis.

Assimilation of GOES-8 data in the target area west of 40W strengthens the main upper level jet and associated PV, but the forecast impact is minimal and the spatial structure of the forecast difference in sea level pressure (Fig. 4c) differs significantly from the control forecast error (Fig. 1). In this case, the forecast error norm is reduced by only 4%. In contrast, assimilation of GOES-8 data in the target area east of 40W produces a significant change to the lower tropospheric temperature in the strongly sensitive region of the cyclone warm sector, but makes little or no change to the main upper level jet and PV anomaly. In this case, the forecast sea level pressure difference is approximately three times stronger than in the west-of-40W assimilation, and the spatial structure of the forecast difference in sea level pressure is very similar to that of the control forecast error (Fig. 1). The east-of-40W assimilation reduces the forecast error norm by 20%, which is roughly comparable to the error reduction obtained by assimilating GOES-8 winds over the entire target area (70W-10W, 45N,60N). These results suggest that correction of analysis errors in the lower tropospheric thermal field (rather than correction of errors associated with upper tropospheric features) can have the greater impact on the improvement of cyclone forecasts.

The largest positive impact is obtained by assimilating both the G-IV dropsonde data and the GOES-8 winds in the large target area (70W-10W, 45N,60N). In this case, the magnitude of the sea level pressure change is similar to that obtained by assimilating the G-IV data alone, but the spatial pattern of the correction (not shown) more closely resembles that of the control forecast error. This improvement is reflected by a 38% decrease in the forecast error norm, as shown in Table 1.

The results of these experiments can be understood in terms of the forecast error projection onto the

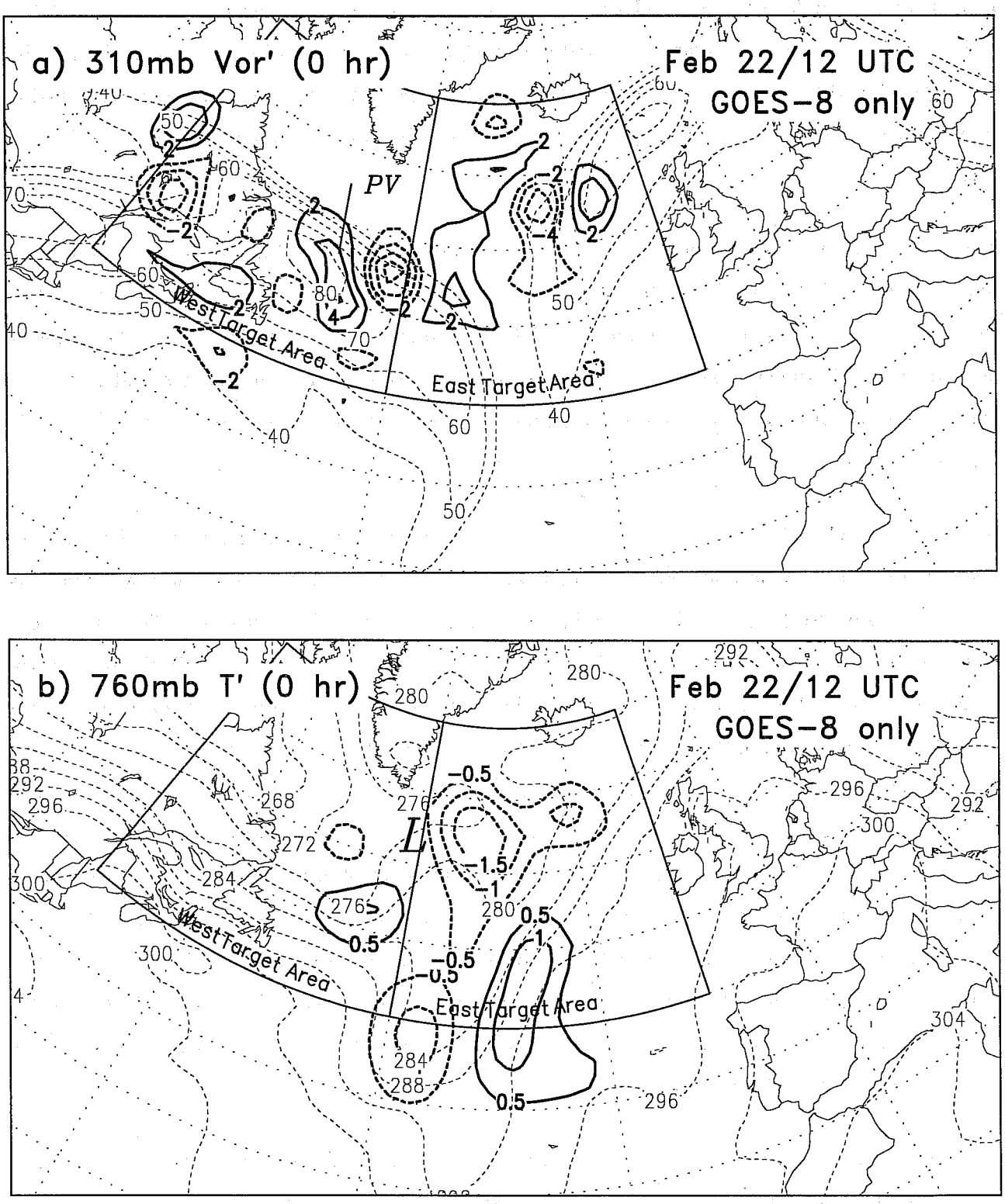

Fig. 4 Analysis increments of (a) vorticity at 310 hPa (bold contours, 2×10^{-5} s^{-1}) and (b) temperature at 760 hPa (bold contours, 0.5 K) due to assimilation of GOES-8 winds on 22 Feb 1200 UTC. Change in 24-hour forecast sea level pressure (0.5 hPa) on 23 Feb 1200 UTC resulting from assimilation of GOES-8 winds in (c) west target area only, including upper level PV anomaly (marked), and (d) east target area only, including cyclone warm sector. Light dashed contours are (a) wind speed (ms^{-1}) at 310 hPa, and (b) potential temperature (K) at 760 hPa. Box outline in (c) and (d) is forecast verification area.

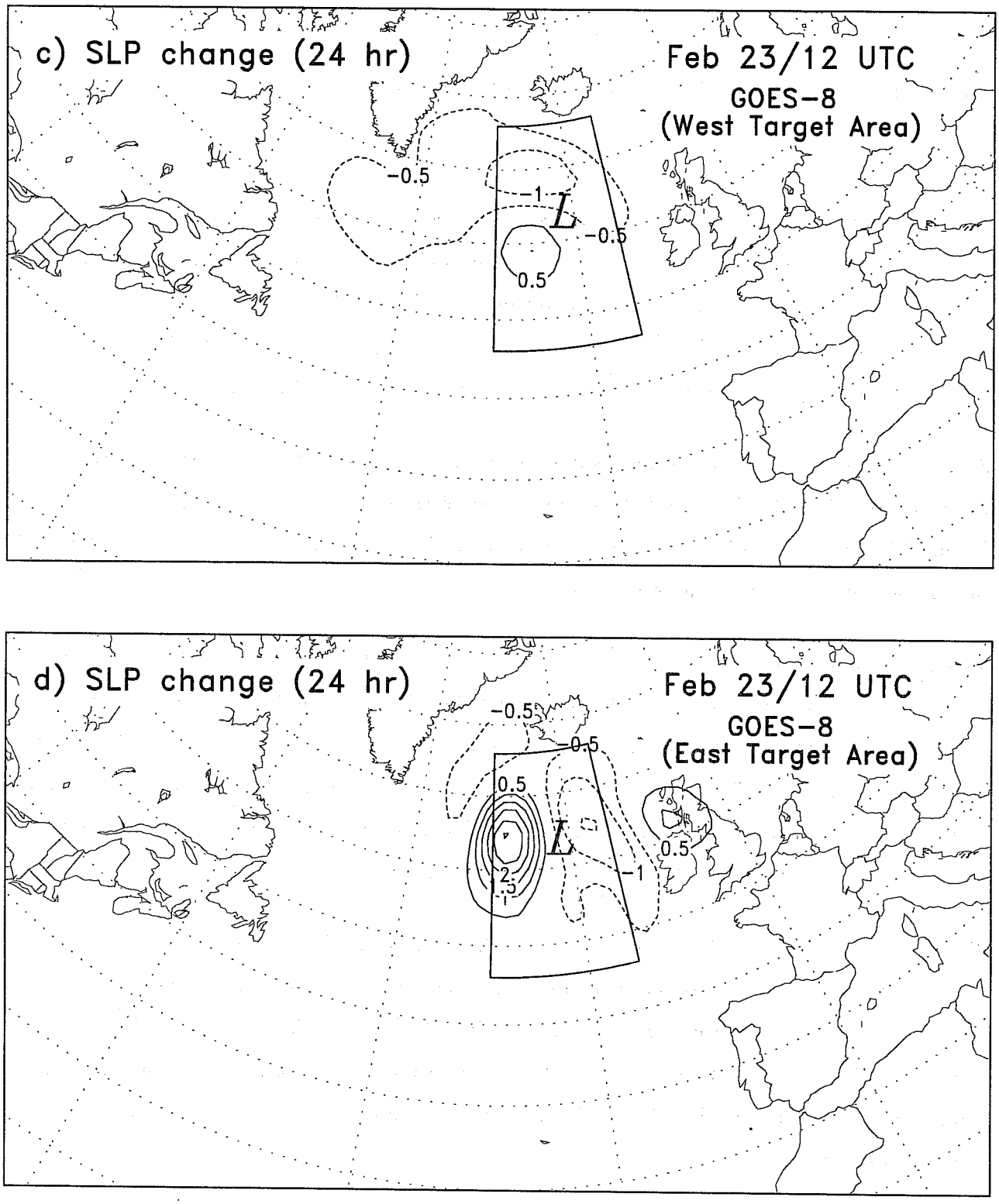

Fig. 4 (continued)

target SVs

$$\tilde{\mathbf{e}}_t = \mathbf{C}^{-1/2} \sum_i d_i \, \mathbf{v}_i \,, \tag{9}$$

where $\mathbf{v}_i$ is an orthonormal SV at the forecast verification time and

$$d_i = < \mathbf{C}^{1/2} \mathbf{v}_i \,;\, \mathbf{e}_t > \tag{10}$$

is a projection coefficient. Fig. 5a shows the projection coefficients of the five leading SVs in the control, G-IV, GOES-8 (large target area) and combined G-IV plus GOES-8 assimilation experiments. First, we note that the control error projects roughly equally onto SV#1 and SV#3, with a somewhat weaker projection onto SV#5 (although, we focus our analysis on SV#1 and SV#3 based on their larger growth rates). There is very little projection onto SV#2 and SV#4.

Assimilation of the G-IV data alone reduces the error projection onto SV#1, while increasing the projection onto SV#3. Clearly, SV#2 and SV#4 play little or no role in describing the forecast error in the FVA since the G-IV data significantly increase the error projection onto these SVs but still produce a significant forecast improvement.

Assimilation of the GOES-8 winds in the large target area has little impact on SV#1, but significantly decreases the error projection onto SV#3. Considering the results in Table 1 for this experiment, it appears that reducing the error projection onto SV#3 also plays a significant role in improving the forecast. This is confirmed by examining the projection coefficients for the combined G-IV plus GOES-8 assimilation experiment, which show a significant decrease in the projection onto both SV#1 and SV#3, thus providing the best overall forecast improvement.

Table 5b compares the projection coefficients for the control, GOES-8 (large target area), GOES-8 west-of-40W and GOES-8 east-of-40W assimilation experiments. As expected based on the above, the different forecast results in these experiments (see Table 1) can be explained primarily in terms of the error projection onto SV#3. In summary, the results in Fig. 5b strongly suggest that reducing the initial error projection onto SV#1 and SV#3 in the target area lead to a significant improvement in forecast skill in the FVA.

3.2 FASTEX IOP-17

IOP-17 presents one of the most dramatic cases of explosive cyclogenesis during FASTEX, with a developing cyclone south of St. John's, NF on 17 Feb 1800 UTC at 1015 hPa deepening to 953 hPa off the northwest coast of Ireland on 19 Feb 1200 UTC. This was also one of the most difficult cases from a

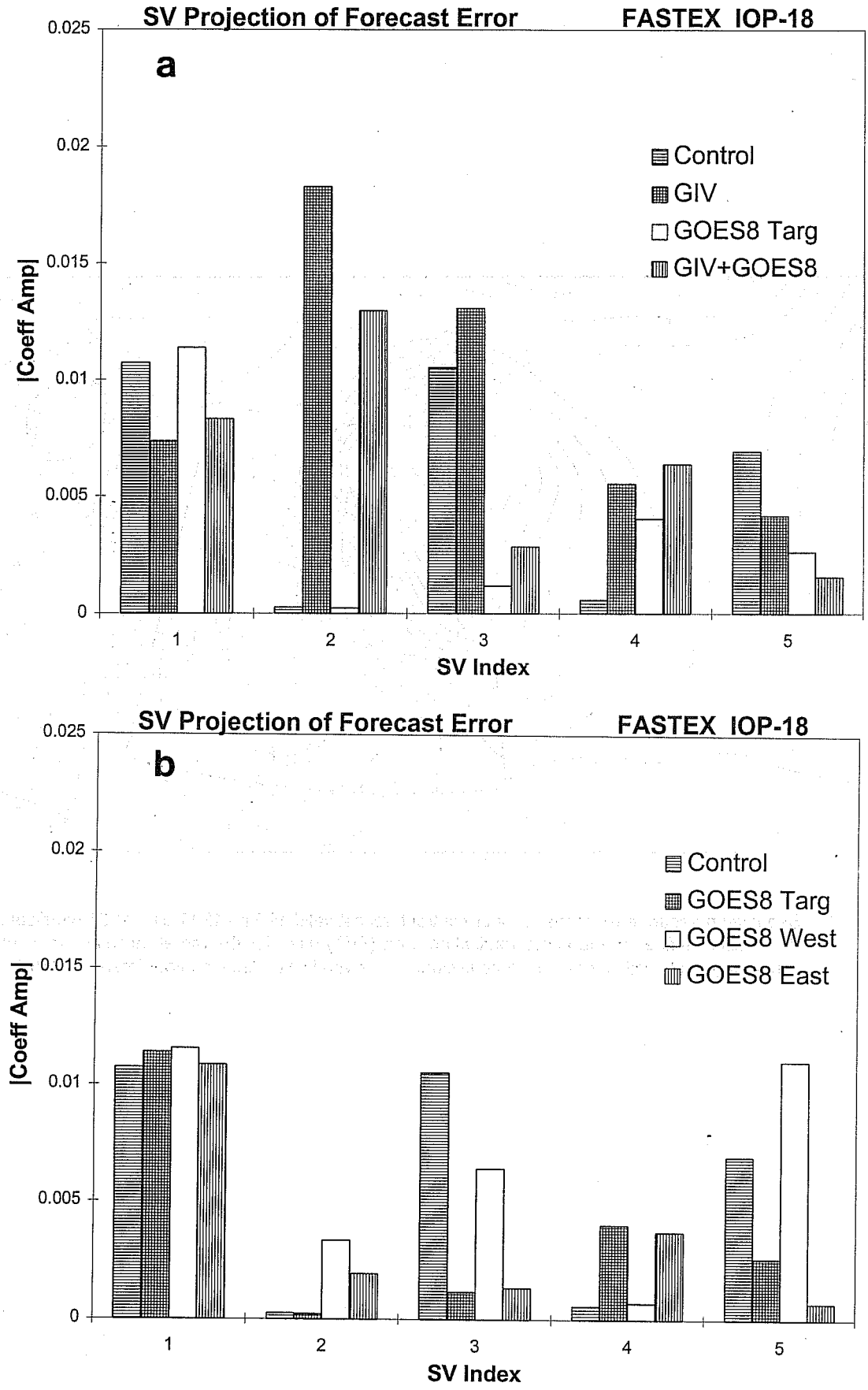

Fig. 5 Forecast error projection onto first five leading (target) SVs for data assimilation experiments in IOP -18 (see legends and text for details).

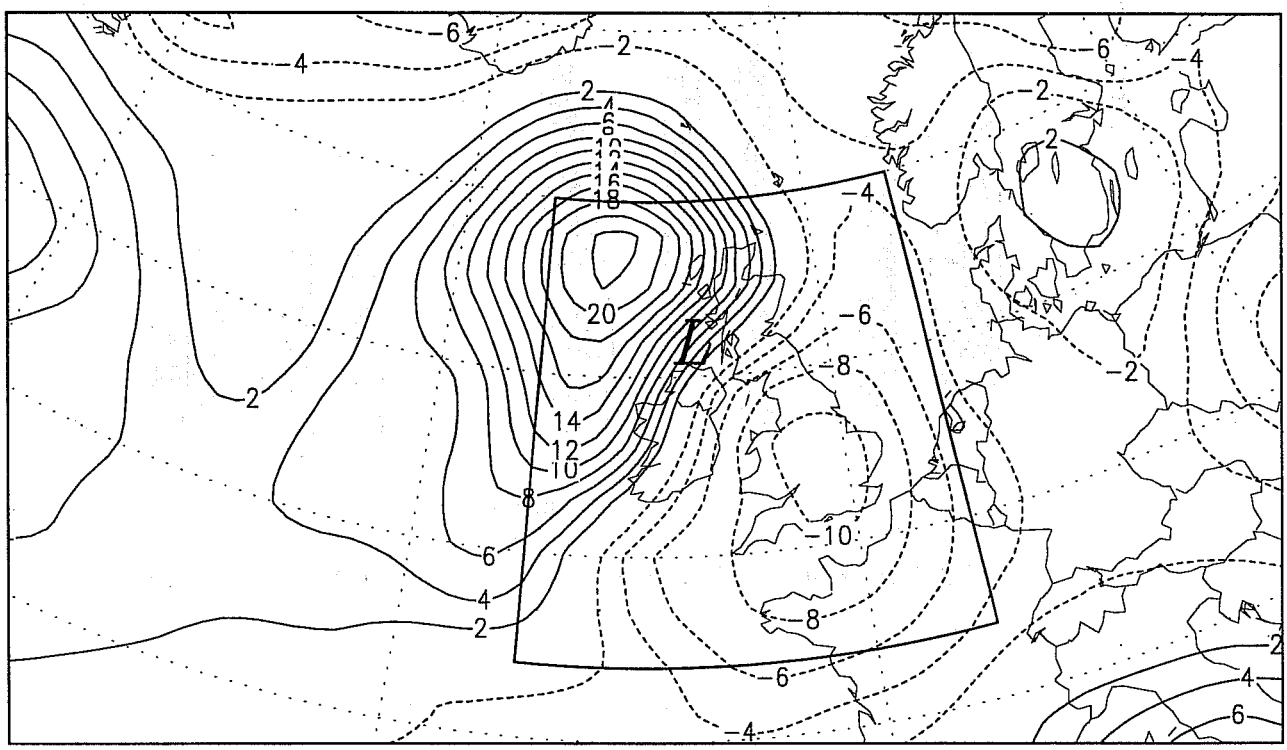

Fig. 6 Sea level pressure error of the 42-hour control forecast valid 19 Feb 1200 UTC 1997 (verification time). Box outline defines the forecast verification area (FVA) used for the target calculations; L marks the control forecast position of the surface cyclone at the verification time; contour interval is 2 hPa.

targeted observing perspective due to the cyclone's complex synoptic structure and rapid amplification during the initial stages of the forecast, and because logistical constraints prevented the G-IV from sampling the most important sections of the adjoint-based target area.

The control forecast for this case was run from initial conditions on 17 Feb 1800 UTC produced from a 6-hr data assimilation cycle containing no special FASTEX data during the previous 36 hours. The control forecast sea level pressure error is greater than 20 hPa on 19 Feb 1200 UTC due to an under-deepening and eastward shift of the cyclone center (Fig. 6). The verifying analysis at this time contains some special FASTEX data.

Fig. 7a,b show the temperature and vorticity components at 680 hPa for SV#1 on 17 Feb 1800 UTC; this is considered the dominant target structure for this case owing to its large amplification rate (16.3) compared with SV#2 (11.0) and SV#3 (7.0). It might be noted that the SV amplification rates for this case were among the largest of any FASTEX IOP with a comparable optimization period, consistent with the explosive development of the cyclone. The target calculations were produced from an analysis on 16 Feb 1200 UTC, allowing a 30-hour lead time for deployment of observational resources. The FVA was chosen to be the volume 15W-5E, 47N-60N, 150 hPa-surface based on the control forecast position of the cyclone on 19 Feb 1200 UTC. The primary observational target area (75W-50W, 30N-50N) is roughly defined to include the extrema of both temperature and vorticity for SV#1, which occur in the layer 600-800 hPa.

Figs. 8a,b show the increments of 680 hPa temperature and vorticity, respectively, which result from the assimilation of the G-IV dropsonde data on 17 Feb 1800 UTC. Note that the G-IV data produce a strong (> 3K) negative temperature increment which lies mostly outside the primary observational target area. Assimilation of the G-IV data leads to a 7 hPa decrease in the forecast sea level pressure near, but still to the east of, the analyzed cyclone center on 19 Feb 1200 UTC, coupled with an increase in sea level pressure in a zone extending southeastward along the trailing cold front (Fig. 8c). A comparison of these differences with the control forecast error in Fig. 6 reveals significant deficiencies in the horizontal structure and orientation of the G-IV data impact, especially in the frontal zone where the change in sea level pressure is actually of the incorrect sign. Indeed, the forecast error energy norm (Table 2) shows a 20% *increase* relative to the control forecast in this case.

The negative impact of the G-IV data may indicate a potential danger of having inadequate (partial) data coverage of target areas, especially when the first guess is of poor quality. In this case, the sea level pressures of the dropsonde data in locations well to the northeast of the cyclone center were

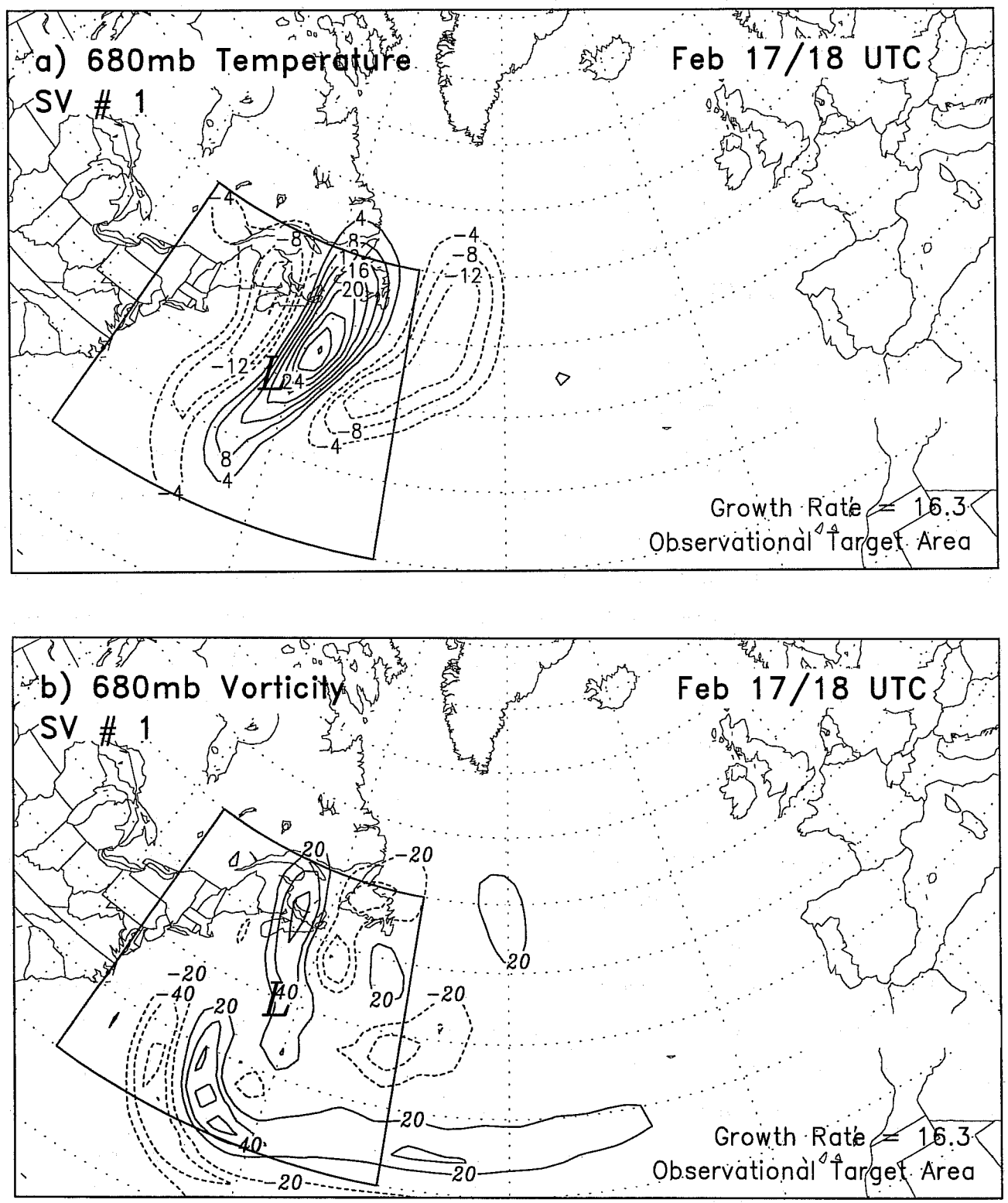

Fig. 7 Target SV#1 (a) temperature and (b) vorticity components at 680 hPa, valid 17 Feb 1800 UTC 1997 (target time). Box outline defines the primary observational target area; L marks the position of the surface cyclone at target time; contour interval is 4 K in (a) and 20×10^{-5} s^{-1} in (b).

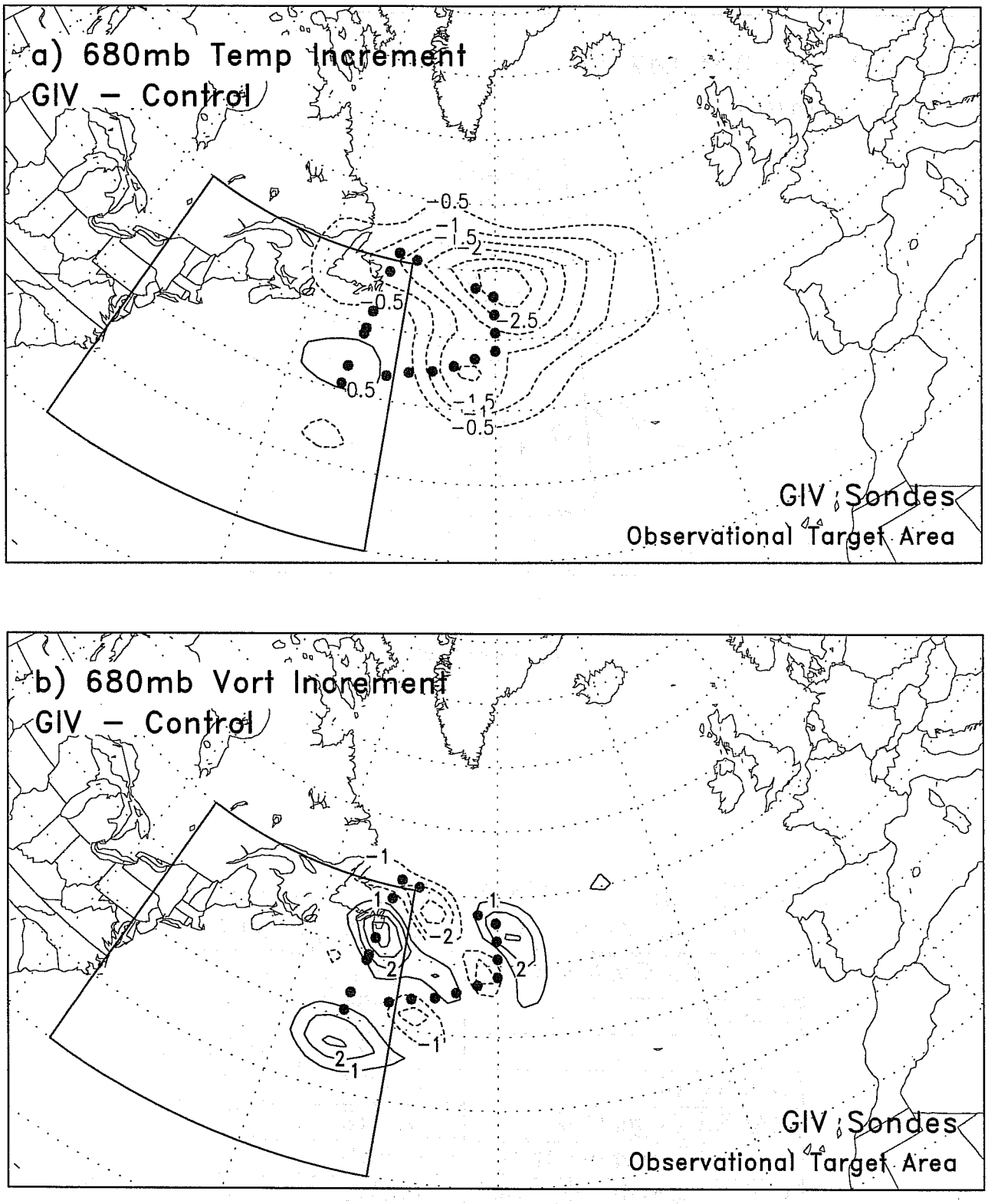

Fig. 8 Analysis increments of (a) temperature and (b) vorticity at 680 hPa due to assimilation of G-IV dropsonde data (solid dots) on 17 Feb 1800 UTC; (c) resulting change in 42-hour forecast sea level pressure on 19 Feb 1200 UTC. Contour interval is 0.5 K in (a), 1×10^{-5} s^{-1} in (b) and 1 hPa in (c). Box outline is primary observational target area in (a) and (b), and forecast verification area in (c).

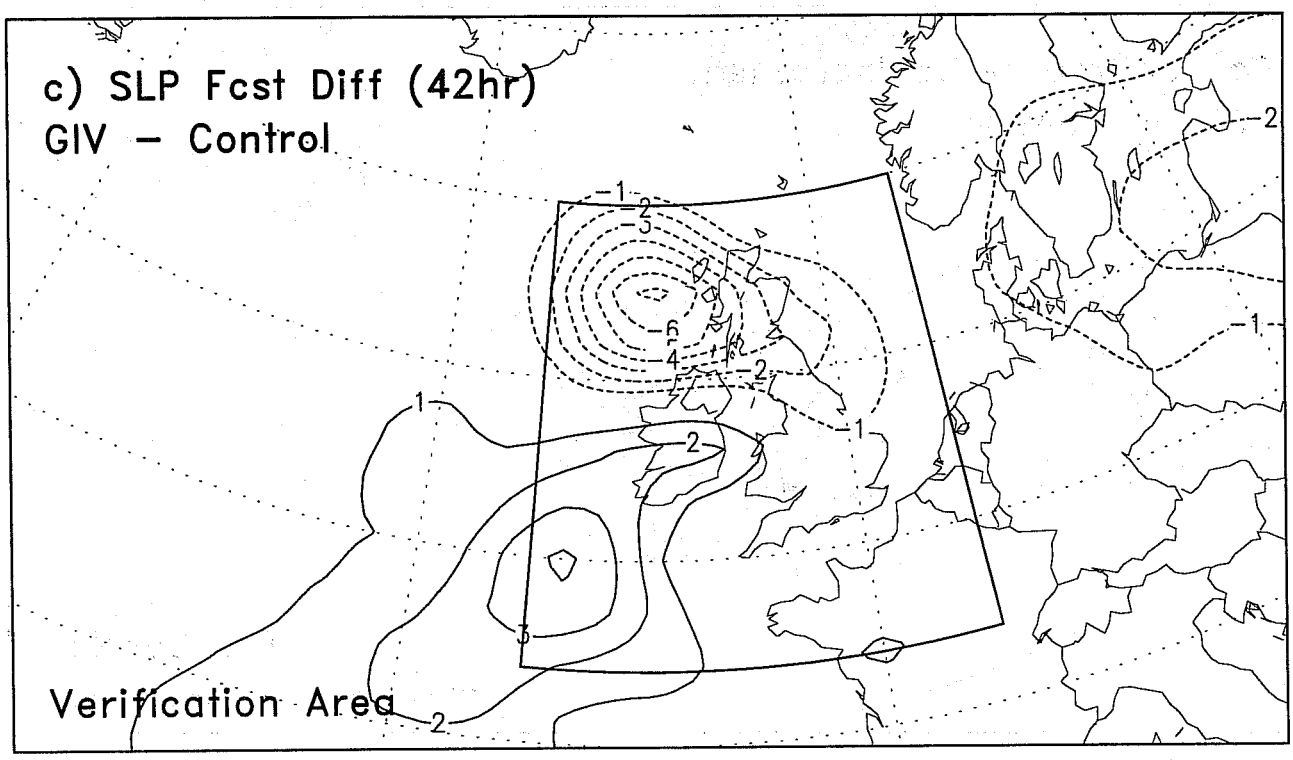

Fig. 8 (continued)

FASTEX IOP-17 17Feb 18UTC - 19Feb 12UTC

Forecast Verification Area: 15W-5E, 47-60N

Initial Conditions	ε_{42} (m^2s^{-2})	$\Delta\varepsilon_{42}$ (%)
Control	0.6777	---
GIV	0.8123	+20
GOES8 All	0.6723	-1
RAOBS Target (18Z)	0.5318	-22
RAOBS Target (6+18Z)	0.4960	-27
GOES8+RAOB+SHIP Null	0.6342	-6

Table 2: As in Table 1, except for IOP-17.

considerably lower than the surrounding values in the first guess field. This resulted in an erroneous northeastward displacement of the low level circulation in the analysis. The problem was exacerbated by the fact that the dropsonde data are weighted heavily in the analysis scheme. No attempt has been made to adjust these weights in the analysis scheme, although this will be investigated in the future.

Attempts to supplement the G-IV dropsonde data using GOES-8 winds were also frustrated by a lack of coverage in key parts of the target area. Extensive cloud cover associated with the already well developed closed circulation of the cyclone on 17 Feb 1800 UTC restricted the retrieval of mid-lower tropospheric GOES-8 winds in these locations. As a result, assimilation of all available GOES-8 wind data produced a nearly neutral forecast impact (Table 2).

As a second alternative data source for this case, we examined the impact of special FASTEX RAOB ascents at off-synoptic times. Special ascents took place at 0600 and 1800 UTC (and sometimes more frequently) during most IOPs. Figs. 9a,b show the temperature and vorticity increments produced by assimilating RAOB data at five locations inside the target area (namely, St. John's, Sable Island, Chatham, Wallops Island and Bermuda) on 17 Feb 1800 UTC, without inclusion of the G-IV or GOES-8 observations. Note the better correspondence of the increments with the extrema of SV#1 (Fig. 7) compared with those produced by assimilation of the G-IV data (Fig. 8). In particular, there is better coverage of target structures in the central and southern parts of the target area. Assimilation of the RAOB data leads to a moderate decrease in the forecast sea level pressure of approximately 5 hPa near the cyclone center on 19 Feb 1200 UTC (Fig. 9c). However, the overall structure of the forecast correction in the FVA is now more similar to that of the control forecast error. In this case, there is a 22% reduction in the forecast error norm in the FVA (Table 2).

Given the proximity of coastal RAOB stations relative to the target area, an interesting question is whether the assimilation of special data in near upstream locations at a previous analysis time augments the targeting at 1800 UTC. To investigate this, the control analysis cycle was re-started from 17 Feb 0000 UTC and special RAOB data were assimilated at five locations on 17 Feb 0600 UTC. These included the same stations as included at 1800 UTC, except for the inclusion of Charleston instead of St. John's based on their respective locations relative to the target area and the fact that the prevailing flow at middle levels was from the west-northwest (not shown) in association with the deepening baroclinic wave. At 1800 UTC, the assimilation of special RAOB data was repeated as in the original experiment.

Figs. 10a,b show the vorticity and temperature increments at 680 hPa on 17 Feb 1800 UTC produced

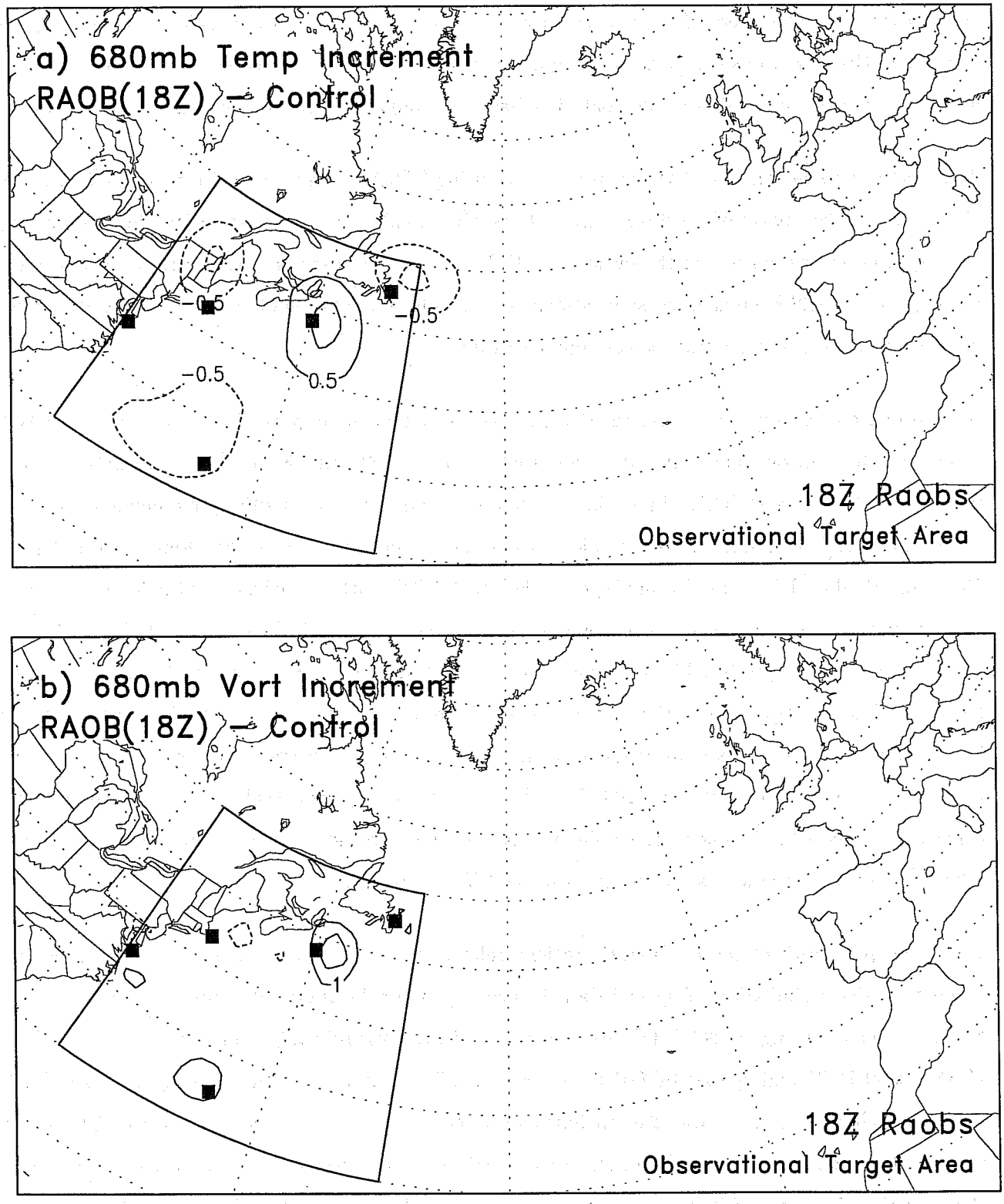

Fig. 9 As in Fig. 8, except for assimilation of special RAOB data (solid boxes) at 1800 UTC.

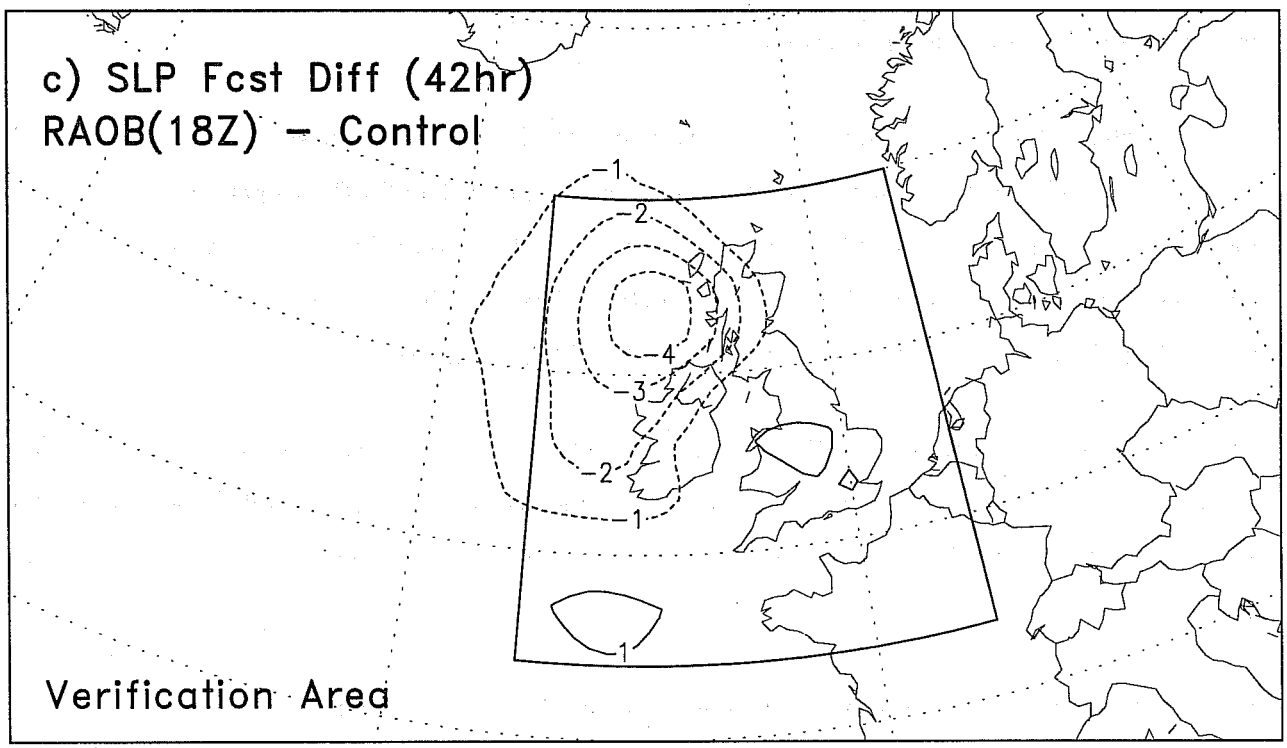

Fig. 9 (continued)

by assimilation of special RAOB data at 0600 and 1800 UTC. The temperature increment is similar to that in Fig. 9a, but shows a more elongated structural definition in the central part of the target area. The vorticity increment, on the other hand, is clearly larger than in Fig. 9b, particularly in the southern part of the target area. This is a region of significant sensitivity, as shown in Fig. 7b. Note that the impacts of the 0600 UTC special data are focused almost entirely in the target region at 1800 UTC. We note that differences near Iceland and Scotland in these figures result from the divergence of the analysis from the control state between 0600 and 1800 UTC in the vicinity of a rapidly deepening cyclone (IOP-16). These increments were subsequently shown to have no discernible interaction with or impact on the case study in question.

Fig. 10c shows the forecast impact of the two-time-level assimilation of special RAOB data. The forecast sea level pressure near the cyclone center is now more than 8 hPa deeper than in the control forecast. Again, the structure of the correction matches well the control forecast error, with further improvements in the forecast over England and Northern France. These improvements are also reflected by a 27% reduction in the forecast error norm in the FVA (Table 2).

The results of other data assimilation experiments for this case are also summarized in Table 2. In particular, we note that a null experiment, which included assimilation of all GOES-8 winds plus land- and ship-based RAOB data outside the primary target area, reduced the forecast error norm by only 6%.

Again, the results of these experiments can be understood in terms of the forecast error projection onto the target SVs. Fig. 11 shows the projection coefficients for the five leading SVs for each experiment. In this case, the forecast impacts can be understood almost entirely in terms of the error projection onto SV#1; in fact, the forecast error norm values shown in Table 2 can be ranked accordingly. For example, note that assimilation of the G-IV data actually increases the error projection onto SV#1 compared with the control forecast, consistent with the increase in the forecast error norm shown in Table 2. In contrast, the assimilation of special RAOB data in the target area at 1800 UTC decreases the error projection onto SV#1, consistent with a reduction in the forecast error norm by 22%. Assimilation of special RAOB data at 0600 and 1800 UTC produces a further decrease in the error projection onto SV#1, consistent with a further reduction in the forecast error norm of 27%. Note that all three assimilation experiments significantly decrease the error projection onto SV#2. However, this effect is clearly of secondary importance, as can be inferred, for example, by comparing the projection coefficients for SV#1 and SV#2 in the G-IV and 1800 UTC RAOB assimilation experiments.

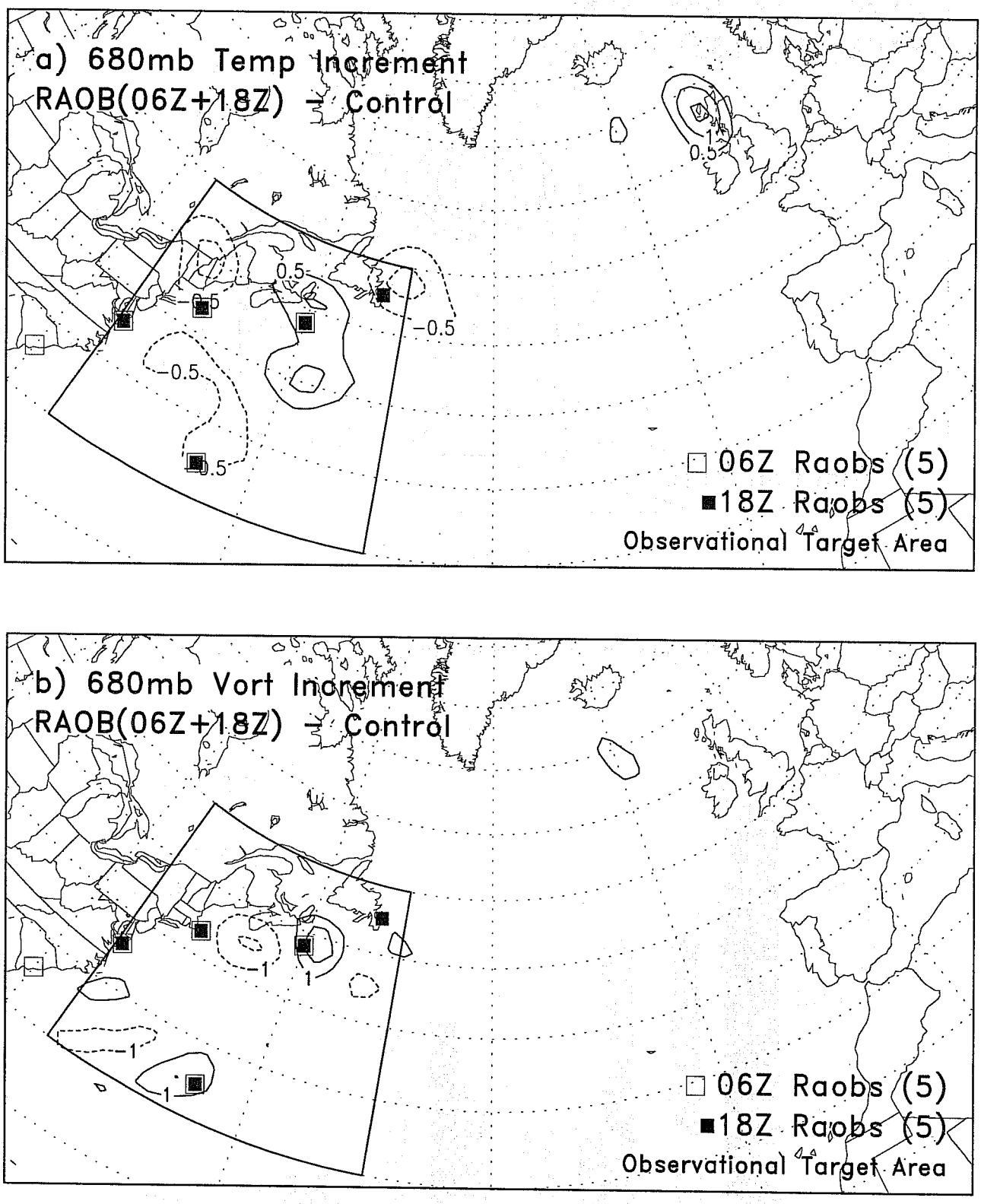

Fig. 10 As in Fig. 8, except for assimilation of special RAOB data at 0600 UTC (open boxes) and 1800 UTC (solid boxes).

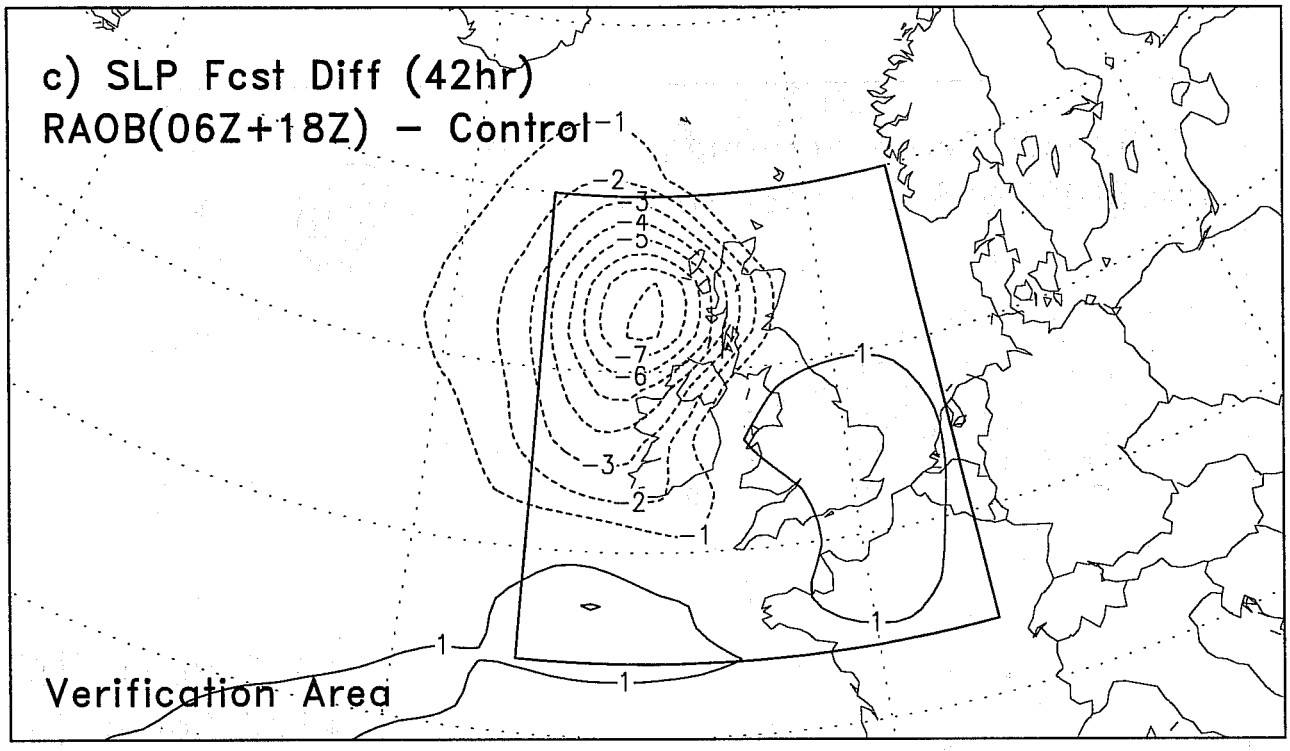

Fig. 10 (continued)

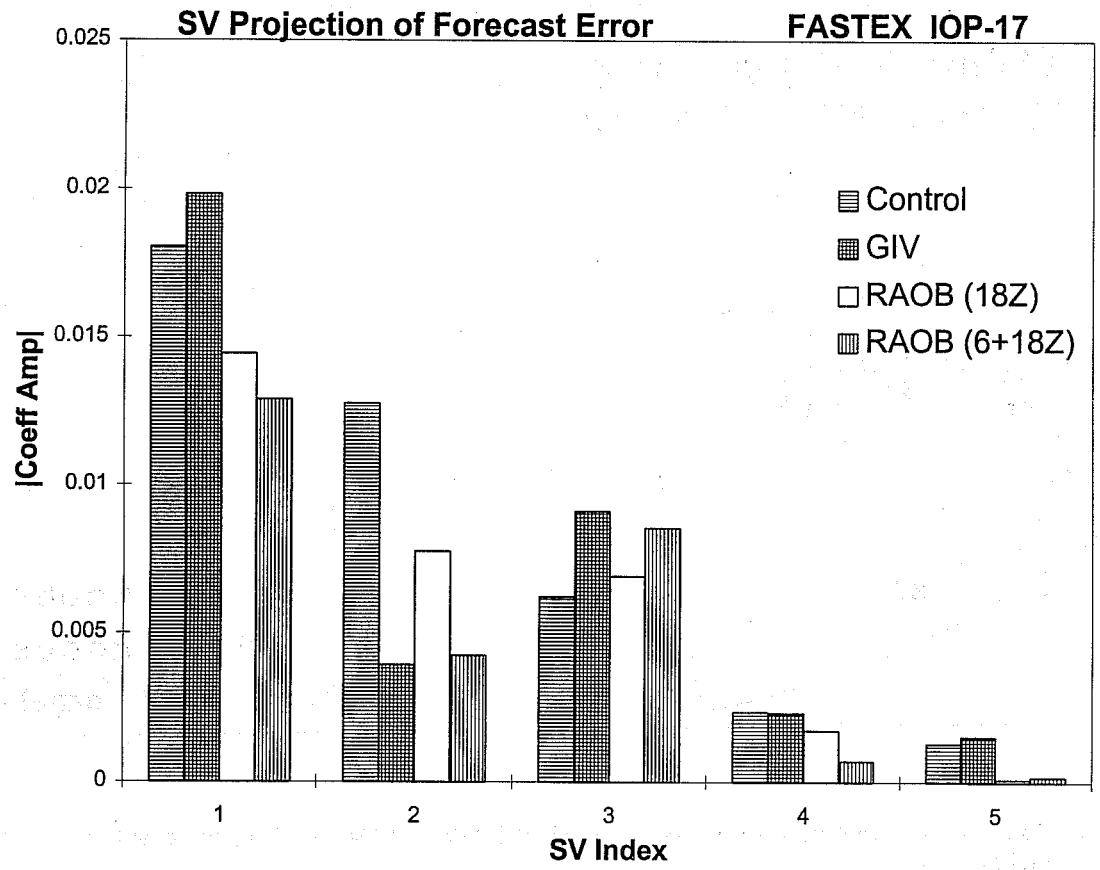

Fig. 11 As in Fig. 5, except for IOP-17.

In summary, assimilation of data in the adjoint-based target area had a significant impact on the cyclone forecast in IOP-17, which can be interpreted to a large extent by the reduction of initial condition errors which project onto the leading target SV. Again, however, partial data coverage in the target area appears to be a significant limiting factor in these results.

4. SUMMARY AND DISCUSSION

The results of this study demonstrate that adjoint-based singular vectors and sensitivity information can be used effectively as the basis of a real time adaptive observing strategy. Assimilation of additional observations in upstream sensitive locations identified by the leading SVs of the NOGAPS forecast model produced significant improvements (20–40% reductions in appropriate measures of error) in one- to two-day forecasts of extratropical cyclones during two FASTEX IOPs. The following are the major conclusions and implications of this study.

(i) The assimilation of dropsonde, satellite wind and RAOB data shows that model analysis errors do in fact occur in sensitive locations identified by singular vectors and adjoint sensitivity patterns, and that reducing analysis errors in these locations can control a significant fraction of the forecast error in the verification area. In contrast, assimilation of additional data outside the target area has relatively little impact in the verification area. In both IOPs examined, a significant positive forecast impact was obtained by reducing initial condition errors at middle to lower levels in the area of the cyclone warm sector.

(ii) The forecast impacts of the additional data can be explained in terms of the analysis error projections onto the leading (target) SVs. In a more general sense, these results indicate that the critical underlying assumptions and approximations made in applying the adjoint methodology, including linearization about a time varying basic state, inclusion of simplified model physics in the tangent models, and the use of an energy based metric as an approximation of the true analysis error covariance metric, are appropriate for studying atmospheric predictability on these scales (Palmer et al., 1997; Gelaro et al., 1997).

(iii) Having stated (ii), it should be recognized that improved estimates of the analysis error covariance metric in particular will undoubtedly improve the utility of SV target calculations. For example, in the case of IOP-18, areas of large SV amplitude over eastern Canada were subjectively ignored in defining the critical target area and flight track of the G-IV, based on the known proximity of conventional land based observations. Preliminary studies indicate that SV amplitudes in well observed locations

may be significantly reduced when a metric is used which incorporates information about the true distribution of conventional observations.

(iv) Partial data coverage in the target area appears to be a significant limiting factor on the effectiveness of adaptive observations. At best, the effect of this limited data coverage will be to reduce the potential positive impact of the targeting. In the worst case scenario, there is evidence that partial coverage can actually degrade the forecast. In the case of IOP-17, it was found that the assimilation of G-IV dropsonde data outside the cyclone environment had a significant negative impact on the forecast. This was most likely due to several factors including a poor (weak) representation of the cyclone in the first guess field, combined with heavily weighted dropsonde observations outside the cyclone environment resulting in an erroneous displacement of the low level circulation. We note that a similar result was obtained when dropsonde data from a Lear jet flight in a nearby location several hours later were assimilated into the initial conditions on 18 Feb 0000 UTC.

(v) As a follow on to (iv), it is unlikely that any single observing platform will provide adequate data coverage of entire target areas on a consistent basis. Rather, it remains to define some optimal mix of observations that will provide the most forecast benefit. We note that targeted data from aircraft dropsondes, satellite winds and special RAOB ascents were utilized in the investigation of the two IOPs presented in this paper.

(vi) The use of more advanced data assimilation methods, particularly four dimensional variational (4DVAR) assimilation, is likely to increase the effectiveness of adaptive observations. First, it is well known that the potential impact of aircraft dropsonde and (polar orbiting) satellite data, which are spread over space and time, cannot be fully realized using OI or three dimensional variational (3DVAR) methods. In addition, the assimilation of targeted observations in regions of strong initial condition sensitivity over an extended period (several analysis cycles) is likely to increase their effectiveness. We note that the maximum positive impact on the cyclone forecast in IOP-17 was obtained by a two-time-level assimilation of special RAOB data in, and upstream from, the target area.

5. REFERENCES

Bergot, T, S Malardel and A Joly, 1996: Sensitivity and singular vectors calculation in the operational context of FASTEX. Proceedings of Seventh Conference on Mesoscale Processes, Reading, UK. American Meteorological Society.

Bishop, C H and Z Toth, 1996: Using ensembles to identify observations likely to improve forecasts. Proceedings of Eleventh Conference on Numerical Weather Prediction, Norfolk, Virginia, USA. Amer-

ican Meteorological Society.

Buizza, R, 1994: Localization of optimal perturbations using a projection operator. *Q. J. R. Meteorol. Soc.*, **120**, 1647–1681.

Buizza, R, R Gelaro, F Molteni and T N Palmer, 1997: The impact of increased resolution on predictability studies with singular vectors. *Q. J. R. Meteorol. Soc.*, **123**, 1007–1033.

Errico, R M and T Vukićević, 1992: Sensitivity analysis using an adjoint of the PSU-NCAR mesoscale model. *Mon. Wea. Rev.*, **120**, 1644–1660.

Gelaro, R, R Buizza, T N Palmer and E Klinker, 1997: Sensitivity analysis of forecast errors and the construction of optimal perturbations using singular vectors. To appear in *J. Atmos. Sci.*

Langland, R H, R L Elsberry and R M Errico, 1995: Evaluation of physical processes in an idealized extratropical cyclone using adjoint sensitivity. *Q. J. R. Meteorol. Soc.*, **121**, 1349–1386.

Langland, R H and G D Rohaly, 1996: Adjoint-based targeting of observations for FASTEX cyclones. Proceedings of Seventh Conference on Mesoscale Processes, Reading, UK. American Meteorological Society.

Montani, A, R Buizza and A J Thorpe, 1996: Singular vector calculation for cases of cyclogenesis in the north Atlantic storm-track. Proceedings of Seventh Conference on Mesoscale Processes, Reading, UK. American Meteorological Society.

Palmer, T N, R Gelaro, J Barkmeijer and R Buizza, 1997: Singular vectors, metrics and adaptive observations. To appear in *J. Atmos. Sci.*

Pu, Z, E Kalnay, J Sela and I Szunyogh, 1997: Sensitivity to forecast errors to initial conditions with a quasi-inverse linear model. To appear in *Mon. Wea. Rev.*

Rabier, F, E Klinker, P Courtier and A Hollingsworth, 1996: Sensitivity of forecast errors to initial conditions. *Q. J. R. Meteorol. Soc.*, **122**, 121–150.

Rosmond T E, 1997: A Technical description of the NRL adjoint modeling system. NRL Technical Report, NRL/MR/7532/97/7230. NRL, Monterey, California, USA.

Snyder, C, 1996: Summary of an informal workshop on adaptive observations and FASTEX. *Bull. Am. Met. Soc.*, **77**, 953-961.